small methods
www.small-methods.com

Binder-Free Cnt Cathodes for Li-O_2 Batteries with More Than One Life

Zeliang Su, Israel Temprano, Nicolas Folastre, Victor Vanpeene, Julie Villanova, Gregory Gachot, Elena V. Shevchenko, Clare P. Grey, Alejandro A. Franco, and Arnaud Demortière**

Li-O_2 batteries (LOB) performance degradation ultimately occurs through the accumulation of discharge products and irreversible clogging of the porous electrode during the cycling. Electrode binder degradation in the presence of reduced oxygen species can result in additional coating of the conductive surface, exacerbating capacity fading. Herein, a facile method to fabricate free-standing is established, binder-free electrodes for LOBs in which multi-wall carbon nanotubes form cross-linked networks exhibiting high porosity, conductivity, and flexibility. These electrodes demonstrate high reproducibility upon cycling in LOBs. After cell death, efficient and inexpensive methods to wash away the accumulated discharge products are demonstrated, as reconditioning method. The second life usage of these electrodes is validated, without noticeable loss of performance. These findings aim to assist in the development of greener high energy density batteries while reducing manufacturing and recycling costs.

1. Introduction

The global warming associated with increasing concentrations of heat-trapping greenhouse gases in the Earth's atmosphere increases the urgency to develop and apply greener and more sustainable energy applications.[1] The electrification of the transport and portable electronics sectors, with lithium battery (LIB) technology as a fundamental element, is expanding at high rate, spearheading a broader energy transition toward a fossil fuel-free society. Global LIB production has grown from 75 GWh in 2011 to 400 GWh in 2020 and is expected to exceed 1400 GWh in 2025, accounting for the giga-factories under construction in major economies alone.[2,3] However, based on LIB technology and electric vehicle (EV) market analysis, the Ni and Co demand forecast for 2030 is expected to reach 2.5 times their global production capacity of the year 2016. Recently concerns have been raised about the shortage of these elements due to their geolocation rarity.[4,5]

Simultaneously, there are growing concerns over the disposal/recycling of batteries, as commercial LIB typically have an average lifespan of 8–10 years.[6] Millions of tons of LIBs across the world are expected to exit the market by 2040, increasing pressure for developing end-of-life treatment large-scale processes in a sustainable manner.[7–9] Energy density and coulombic efficiency are no longer the only considerations for developing new LIB formulations. Durability, lifespan, and efficient end-of-life treatment becomes increasingly important aspects of further developments in battery research.[10–12]

Z. Su, N. Folastre, G. Gachot, A. A. Franco, A. Demortière
Laboratoire de Réactivité et Chimie des Solides (LRCS)
Université de Picardie Jules Verne
CNRS UMR 7314, Hub de l'Energie, Amiens, Cedex 80039, France
E-mail: arnaud.demortiere@cnrs.fr

Z. Su, N. Folastre, G. Gachot, A. A. Franco, A. Demortière
Réseau sur le Stockage Electrochimique de l'Energie (RS2E)
CNRS FR 3459, Hub de l'Energie, Amiens, Cedex 80039, France

I. Temprano, C. P. Grey
Yusuf Hamied Department of Chemistry
University of Cambridge
Cambridge CB2 1EW, UK
E-mail: it251@cam.ac.uk

V. Vanpeene, J. Villanova
ID16B ESRF-The European Synchrotron
CS 40220, Grenoble Cedex 9, 38043, France

E. V. Shevchenko
Argonne National Laboratory
Center for Nanoscale Materials
Argonne, Illinois 60439, USA

A. A. Franco
Institut Universitaire de France
101 Boulevard Saint Michel, Paris 75005, France

A. A. Franco, A. Demortière
ALISTORE-European Research Institute
CNRS FR 3104, Hub de l'Energie, Amiens 80039, Cedex, France

The ORCID identification number(s) for the author(s) of this article can be found under https://doi.org/10.1002/smtd.202300452

DOI: 10.1002/smtd.202300452

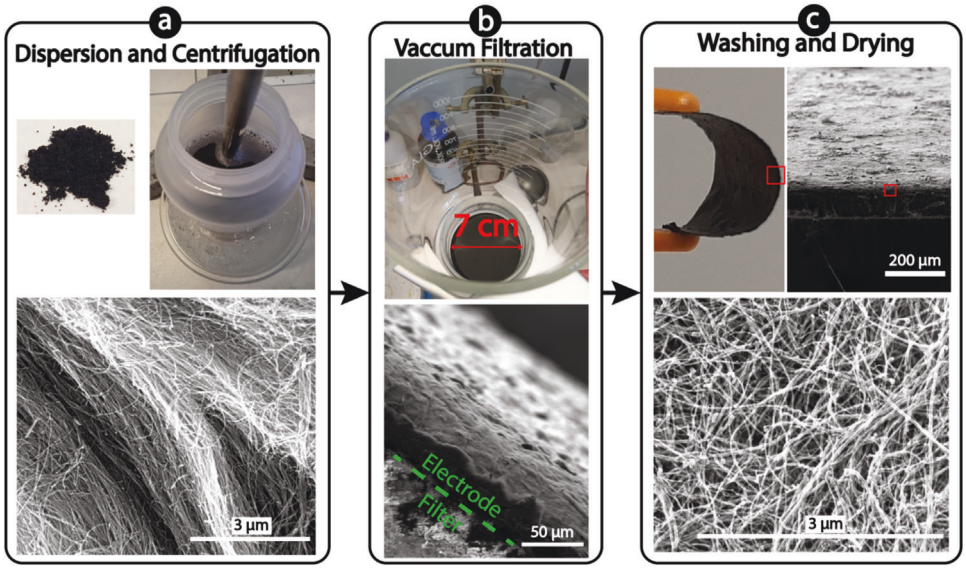

Figure 1. Electrode preparation workflow. a) Optical images of MWCNT powder and ultrasonic probe used for dispersion, and SEM image of the aligned array CNT powder. b) Optical image of a CNT disc on a vacuum filter and SEM image of the filtered material. c) Optical image showcasing the flexibility of the CNT discs and SEM images at different magnifications.

Li-air batteries (LABs) are a potential high-density energy storage system for many novel applications, thanks to their outstanding theoretical energy density (>2920 Wh kg^{-1})[13,14] and relatively low environmental impact compared to LIBs (being transition-metal free). The development of LABs (currently Li-O_2 batteries (LOB), strictly speaking, as most experimental work is performed with pure O_2) is however, currently hindered by cell irreversibility, mainly due to progressive accumulation of discharge products on the air electrode. As electrochemical round-trips progress with relatively low coulombic efficiency, discharge and side products[15–20] accumulate, and the available surface at the electrode diminish,[21] ultimately leading to cell failure. Furthermore, typical polymeric electrode binders, such as Poly(vinylidene fluoride) (PVDF), suffer degradation in the presence of reduced oxygen species resulting in additional coating of the conductive surface, exacerbating capacity fading. Strategies to solve or mitigate these limitations proposed in the literature range from (a) grafting catalysts or doped cathode materials;[22–26] (b) using redox mediators;[27–29] (c) stabilizing the conductive lithium superoxide as discharge product;[20,30] to (d) promoting alternative electrochemistry (such as LiOH), which produces fewer parasitic reactions.[31–33] With these challenges at the forefront of LAB research, key aspects of end-of-life treatment and material recyclability are lagging in the literature.

This work presents a simple and scalable way of preparing self-standing and binder-free air electrodes for LABs, lending them amenable for recycling at end-or-life, using efficient and cost less methods. Thus, highly porous electrodes, based on coiled multiwalled carbon nanotubes (MWCNT) are fabricated, tested, and recycled. The second life capabilities of these electrodes are tested in fresh batteries. We show that the electrochemical performance of the second life material is comparable to the pristine electrodes. The free-standing and binder-free electrodes can be either directly reconditioned or re-dispersed to form new electrodes prior to assembly in new cells. These findings open new routes toward efficient recovery of LAB electrodes for continuous recycling, increasing the potential of LABs as environmentally friendly and low-cost alternative form of energy storage system.

2. Results

2.1. Electrode Fabrication and Microstructural Characterization

The as-purchased MWCNT powder is shown in **Figure 1**a, with nanotube arrays having diameters of 5 to 30 nm and lengths averaging 100 µm. As-received MWCNT powder was initially dispersed in isopropanol and then vacuum filtered, forming a homogeneous disc (Figure 1b). The first filtrate is often of dark color due to a small amount of CNT percolation through the high porosity of the glassy fiber filter, but the filtrate rapidly turns clear, further percolation stopped by the first formed stack of CNTs on the filter paper. It is worth noting that the solvent (isopropanol) can be reused in this process, reducing the total amount of solvent required in the manufacture (and recycling) of these electrodes. In the resulting highly flexible and smearable free-standing disc of entangled CNTs the nanotubes are bundled, as shown by SEM and digital images in Figure 1b,c.

This facile preparation method can produce binder-free electrodes of large dimensions and can be straightforwardly scaled up both in surface area or in thickness, by simply using a bigger funnel (e.g., 7 cm diameter disc shown in Figure 1b) or extending the filtration time (see Figure S1 SEMs in Supporting Information). Throughout the current study, the thickness of the electrode is controlled between 75 to 120 mm, and the electrodes are cut into 1.27 cm diameter discs for electrochemical testing (see Experimental Methods).

The 3D nano-architecture of the so-formed CNT electrodes were characterized using the synchrotron X-ray holo-tomography (nano-CT) technique at the ID16B beamline at the ESRF as described in our previous study.[36] **Figure 2** shows the clear

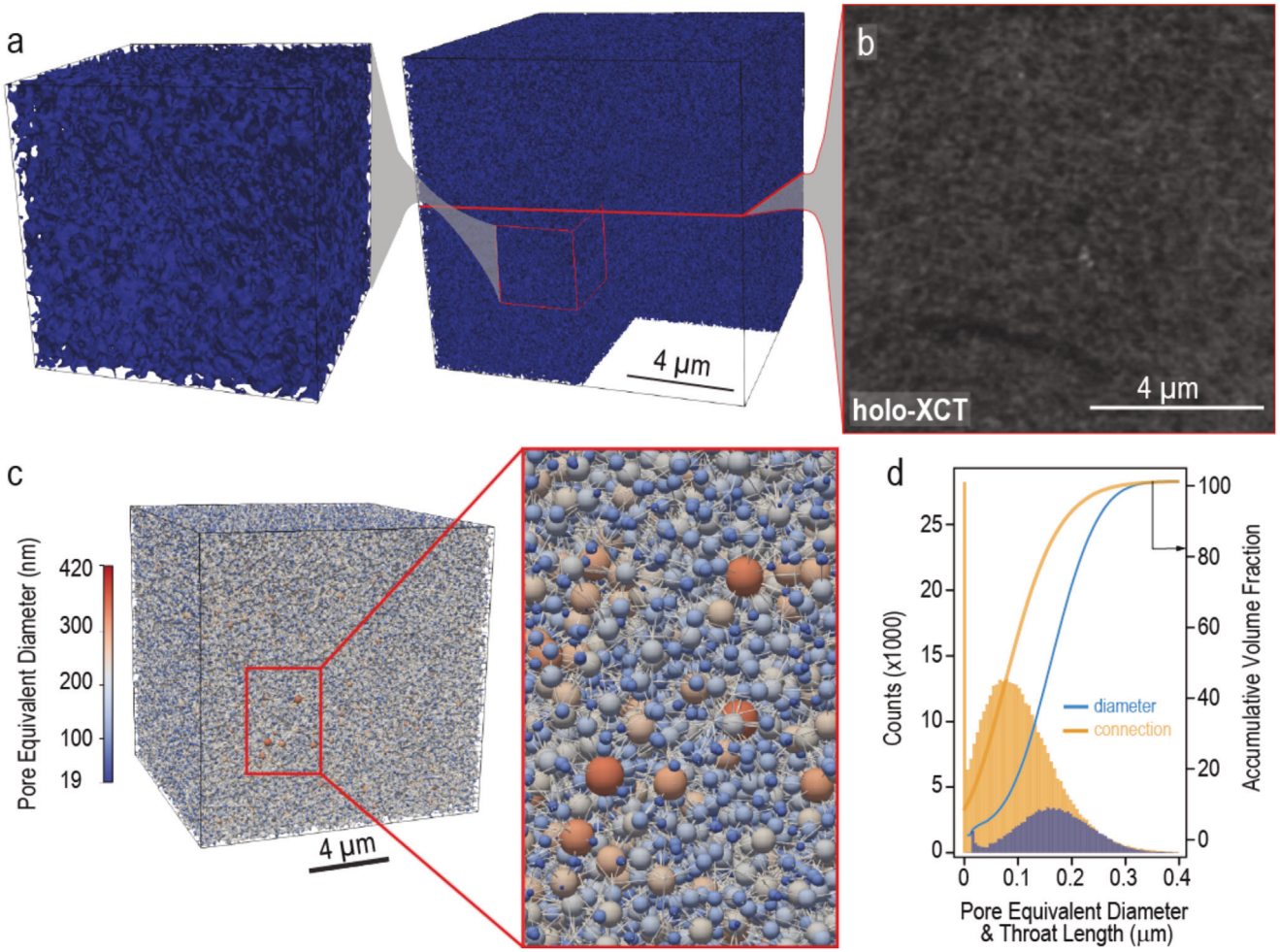

Figure 2. Nano-CT data and structural analysis of binder-free CNT electrodes. a) 3D render of the internal structure of pristine CNT electrodes. b) Cross-sectional slice of the nano-CT data showing the crisscrossed nanotubes. c) Extracted pore-network model of the porous internal structure, where the nodes/balls represent the pores (radii are proportional to pore size, warmer color and larger size of balls indicate larger pores). The sticks represent the inter-connections of these pores (many pores/balls are too small to render). d) The pore equivalent diameter and pore-interconnection distributions of the c) volume.

differentiation obtained between the MWCNT and the pores. From this data, the meso/macro porosity and tortuosity of this material were evaluated at 49% and 1.95, respectively, using the SegmentPy[37] and Taufactor[38,39] softwares (see Figure S2, Supporting Information for the segmentation justification and the representativeness calculation). These porosity and tortuosity values are consistent with those from Li-O_2 binder carbon electrode obtained by FIB/SEM 3D imaging.[35] The porosity of the electrode has a critical impact on the reaction intermediates at the surface while the tortuosity affects the electrochemical kinetics enhancing Li-ion diffusion inside the wetted porous electrode. The pore network distribution of over 400k pores detected in this volume was obtained using Porespy algorithm.[40] It is depicted in Figure 2c with a ball-and-stick model, showing pores and channels respectively. Figure 2d shows the statistical analysis of the porosity from the extracted pore network, indicating that the structure consists in dense small pores and short connections. The values extracted, i.e., average 180 nm in pore diameter and 80 nm in interconnections, revealed a highly connected carbon network with pore diameter close to that found for carbon super-P porous electrode in our previous work.[22]

2.2. Electrochemical Performance

A comparison of stability toward lithium metal for various electrolytes was performed to select the appropriate electrolyte (**Figure 3**a). Li|Li symmetric cells were cycled in commonly reported electrolytes in the LOB literature. Among these, 2 M LiTFSI + 1 M $LiNO_3$ in dimethylacetamide (DMA) showed the most stable behavior, as previously reported by Yu et al.,[43] and thus it was selected as baseline electrolyte for the remainder of this work. Li-O_2 cells with CNT air electrodes and this electrolyte, were tested to determine the total capacity (on deep discharge) and capacity retention evaluation (capacity limited to 500 mAh g^{-1}). Deep discharge tests showed capacities of ≈1480 mAh g_{CNT}^{-1} with a cut-off potential of 2 V (Figure 3b). The stoichiometry of the discharge and charge processes were

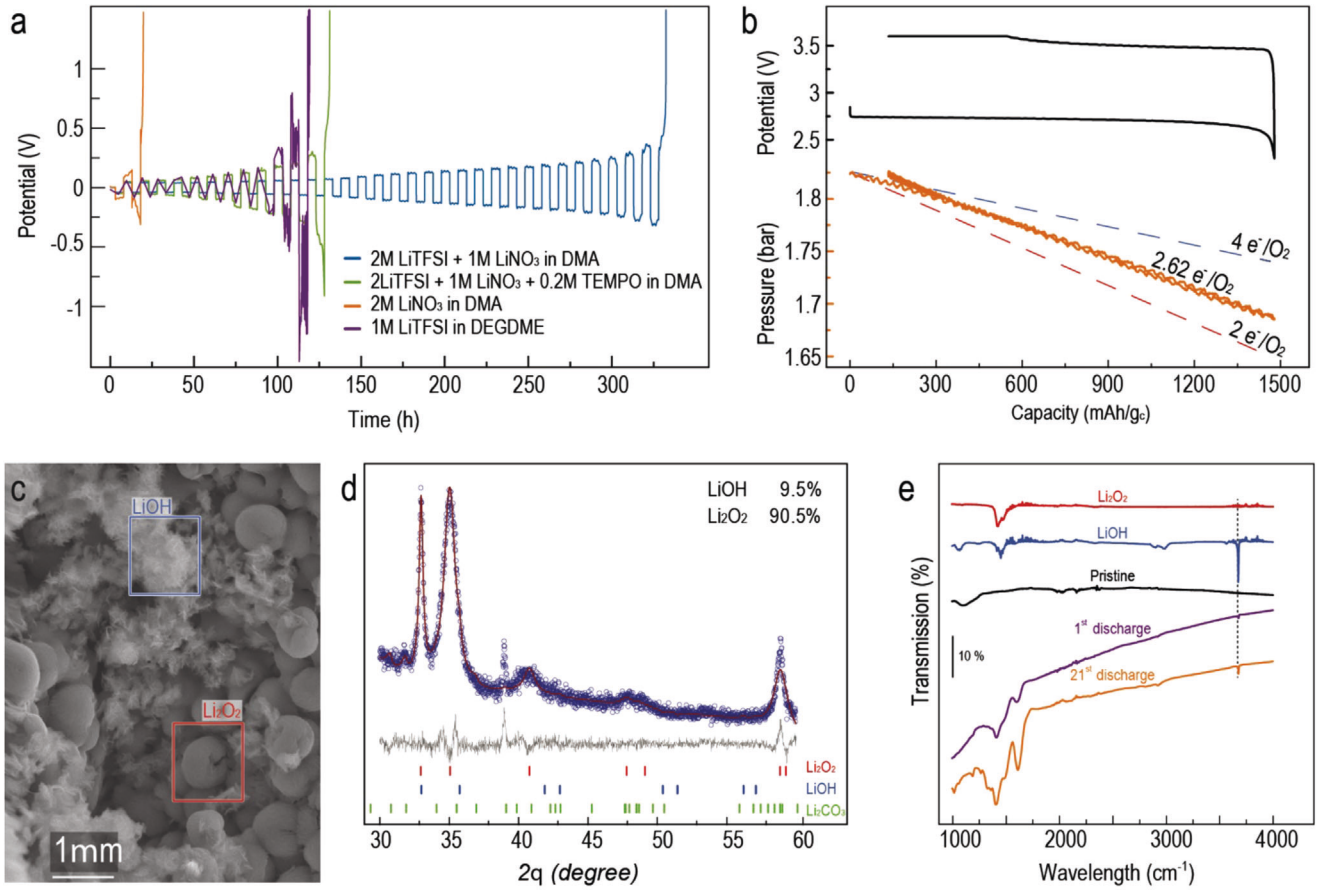

Figure 3. Electrochemistry and discharge products analysis of the first deep discharge. a) Li|Li symmetric cells (200 μA cm^{-2}) containing dimethylacetamide (DMA) with 2 M of LiTFSI and 1 M of $LiNO_3$ (blue); with 0.2 M TEMPO added (green); 2 M $LiNO_3$ (orange); and diethylene glycol dimethyl ether (DEGDME) with 1 M LiTFSI (purple). b) Electrochemical (black) and pressure monitoring (orange) curves of the 1st deep discharge/charge cycle. c) SEM image, d) XRD, and e) FTIR spectra from the air electrode after deep discharge.

evaluated using a Swagelok-based pressure monitoring system[41] (detailed in Figure S2, Supporting Information). During the first discharge, a plateau can be observed at 2.7 V, corresponding to an oxygen reduction process (ORR) with stoichiometry of 2.62 e^-/O_2, as shown in Figure 3a. Such deviation from the expected 2 e^-/O_2 stoichiometry for Li_2O_2 formation would suggest either a substantial amounts of parasitic reactions, or a mixture of discharge products.

SEM post-mortem characterization of the air electrodes after discharge shows an abundance of large toroidal particles (SEM image in Figure 3c) indicative of Li_2O_2 crystals (red square), alongside regions of platelet structures (blue square), reminiscent of small LiOH crystals.[32] XRD data in Figure 3d suggests that the main crystalline product of the discharge is indeed lithium peroxide. The Rietveld analysis indicate that ≈10% of the crystalline phases correspond to lithium hydroxide. FTIR/ATR spectra (Figure 3e), shows a feature assigned to the $\nu_{O\text{-}H}$ mode at 3676 cm^{-1}, further confirming the presence of LiOH in discharged electrodes. The presence of LiOH would explain the deviation from the 2e^-/O_2 stoichiometry expected for Li_2O_2 formation during the ORR, as electrochemical LiOH formation is believed to occur through a 4e^-/O_2 stoichiometry.[32,33] LiOH may form from trace amounts of water (<100 ppm of water measured by Carl Fischer titration) in the electrolyte (see Experimental Methods), or a catalytic effect of the electrode matrix.[42] Overall, the discharge capacity obtained during the discharge process of the CNT electrodes is in accordance with the literature.[43]

During charge, the stoichiometry of the oxygen evolution reaction (OER) is also 2.62 e^-/O_2 up to 3.6 V (Figure 3b), which suggests a highly reversible formation/decomposition of a mixture of discharge products with different stoichiometries (e.g., Li_2O_2 and LiOH).[32,33] Several reports in the literature indicate that hydroxide (in addition to Li_2O_2) formation could be a reversible electrochemical process at relatively low overpotentials due to catalytic effects of either redox mediators,[31,43] solid catalysts,[44] or even hydrophilic CNT-based materials.[42]

In the case of deep discharge cycling (potential limited), a galvanostatic charge process can only recover 60% of the discharge capacity up to 3.6 V before a steep potential slope occurs (Figure S3, Supporting Information). Allowing for the cell potential to rise above 3.6 V results in a reduction in slope of the pressure signal (Figure S3, Supporting Information), indicating that the Oxygen Evolution process (OER) is limited beyond 3.6 V in these cells. To accommodate for the slow kinetics of the OER process at the end of charge, a CC-CV (constant current – constant voltage) protocol, with a potential hold at 3.6 V was thus used

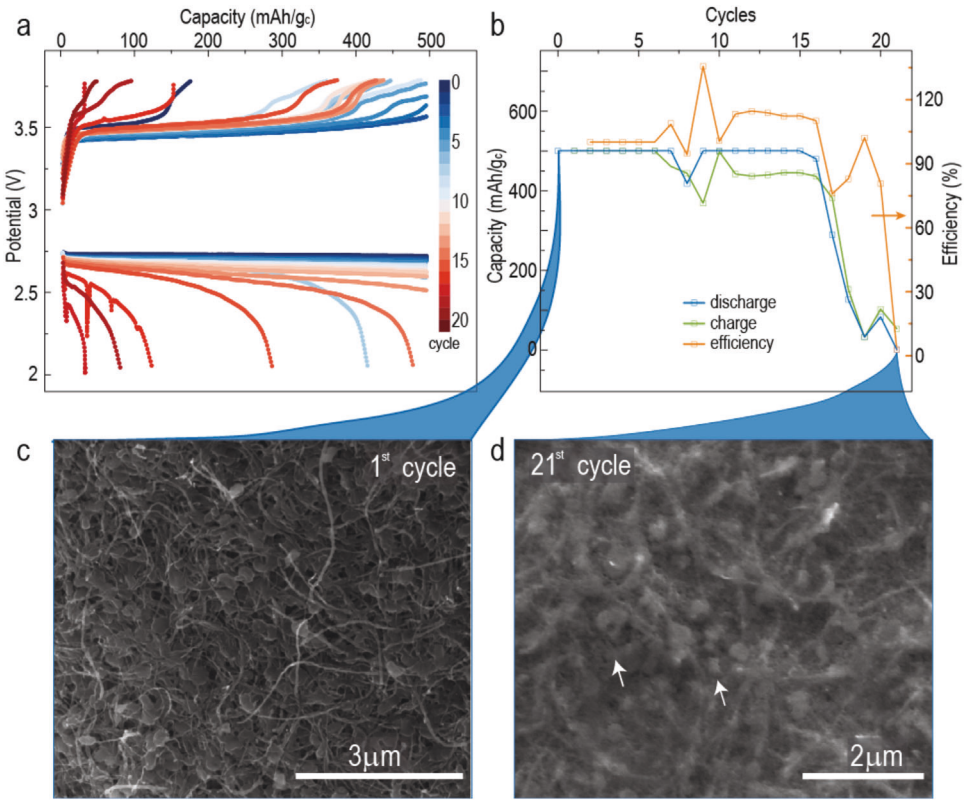

Figure 4. Electrochemical data and SEM images. a) Voltage-capacity profiles of 20 cycles, b) discharge/charge capacities and coulombic efficiency, c) SEM image of the electrode after the first discharge, and d) SEM image of the electrode after 20 cycles.

(Figure S4, Supporting Information) increasing the faradaic efficiency, and thus capacity recovery while limiting the degradation that electrodes can suffer at high potentials.

The CNT-based cells were tested over multiple cycles to a limited capacity of 500 mAh g^{-1} between 2 and 4 V at 40 mA g^{-1}. The characteristic oxygen reduction plateaus at 2.6 V for the discharge process can be observed for up to 15 cycles, whereas the charging plateau at 3.6 V shortens progressively. The reduced capacity recovery during charge results in the accumulation of discharge products, and consequently, a steep drop in the discharge (and charge) capacity from the 16th cycle marks the end-of-life the cell. The previously mentioned CCCV protocol was not used for these cells in order to reach the end-of-life stage at an accelerated rate and study their recyclability.

SEM images of electrodes after 21 cycles (**Figure 4**d) reveal the accumulation of discharge products (EDX analysis in Figure S4, Supporting Information). The morphology of the products is clearly different from the first cycle, with a thick layer of solid covering the surface of the electrode, although toroid- and platelet/flower-like particles can also be found. FTIR/ATR reveals (Figure 3e) an increasing $\nu_{O\text{-}H}$ peak after 21 cycles.

Two possible mechanisms for the origin of cell death were captured in SEM images: pore-clogging (Figure 4d) and surface passivation (**Figure 5**a). The electrode surface presents a typical surface pore-clogging, with solid materials (oxygen- rich as depicted by the Figure S5, Supporting Information) full-filling the free space in-between nanotubes (Figure 4d), while other areas display nanotubes covered by undissolved solids indicating considerable surface passivation (Figure 5a).

2.3. End-of-Life Electrode Treatment

After the cell death, two electrode recovery treatment paths were investigated: 1) reconditioning without further nanotube dispersion and 2) recycling of the CNT material via dispersion and filtration to form new electrodes. For the reconditioning process, an acid and deionized water treatments were investigated, whereas for the CNT recycling process, they had first washed them in abundant deionized water, and then re-dispersed them using the same procedure shown in Figure 1. SEM images show efficient removal of solid deposits by either soaking the aged electrode in a pH = 3 acid solution, or water respectively (Figure 5d,e), and or recycling the CNTs (Figure 5f), (detailed in Experimental Section). EDX data in small magnification over a large area for different electrodes (Figure S5, Supporting Information) confirms the disappearance of oxygen-containing species after washing.

Figure 5b shows Raman spectra of cycled electrodes after acid treatment at different pH values. The two characteristic bands (D at 1338 cm^{-1}, G at 1550 cm^{-1}) correspond to the disorder and in-plane order vibration in the CNT. The ratio between the under-peak area of these bands stays unchanged, indicating no deleterious effect to the bulk structure of the CNT tubes after washing with either hydrochloric or sulfuric acid (pH = 1–4).

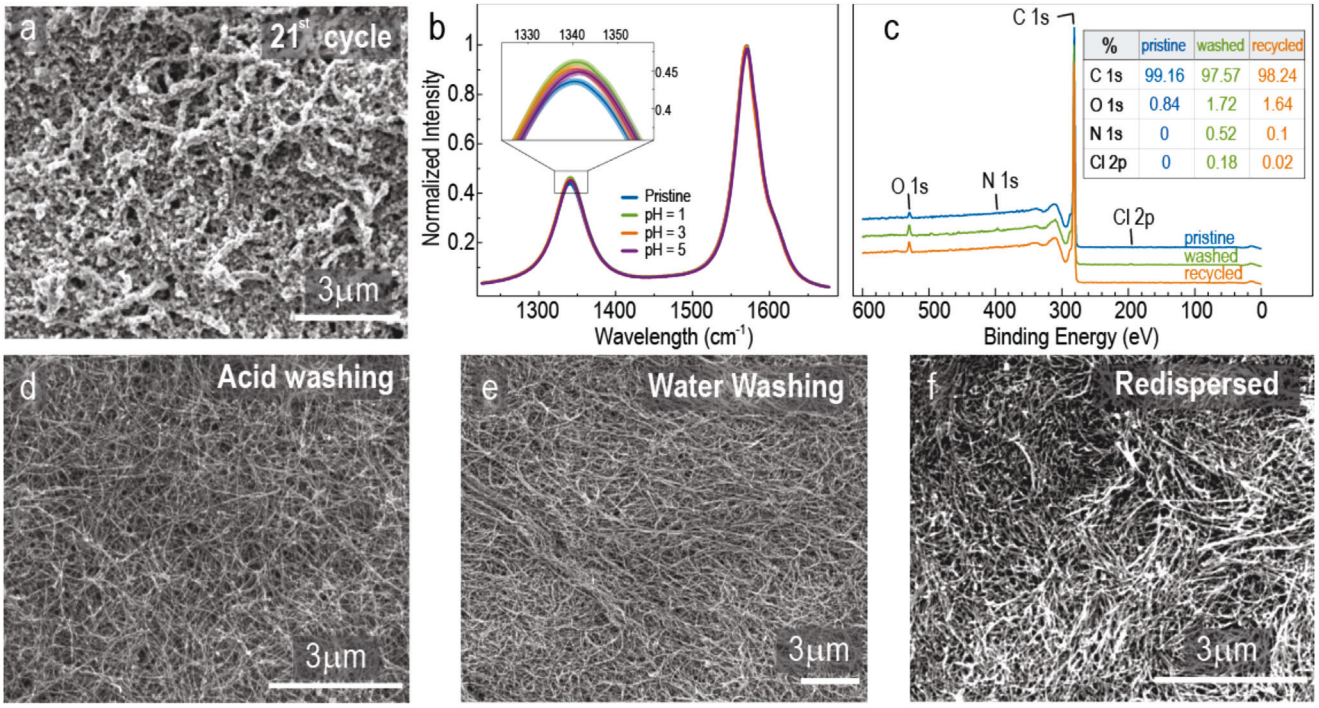

Figure 5. Characterization of recovered electrodes. a) SEM image of the surface of an electrode after 21 cycles. b) A Raman study of the acid washing solvent shows no impact of acid onto the bulk CNT. The characteristic CNT D/G bands ratio remains steady at various pH. c) Surface study of the acid washing/recycling CNT by XPS. d,e) SEM images of electrodes post-treatment.

XPS data (Figure 5c) similarly shows only negligible increases (<1%) of oxygen and other elements in the washed electrodes compared to the pristine ones, suggesting that the electrochemical reaction and the washing process do not significantly alter the structure or surface of the CNT electrodes.

2.4. Electrochemistry of Second-Life Electrodes

The electrochemical performance of electrodes after reconditioning and recycling were investigated under the same galvanostatic cycling conditions (**Figure 6**a–f). Both the discharge and charge plateaus remain 2.6 and 3.5 V respectively, with a polarization of ≈0.9 V. The efficiency plots showed similar electrochemical performance of the second-life electrodes compared to the initial pristine CNT electrodes (Figure 4a). The capacity retention slowly decreases for the first 15 cycles before an acute drop, due to the fading clogging and passivation mechanisms discussed above.

XRD data of treated electrodes (water-washed and recycled) were analyzed prior to and after 1st deep discharge (Figure S6, Supporting Information). Reflections in the 30–60 two-theta region indicate the presence of crystalline discharge products (Li_2O_2, LiOH and Li_2CO_3) in the cycled electrodes. Only minor differences can be observed between the spectra of the pristine, water washed, and recycled electrodes, indicating that the electrochemical products were not impacted by the recondition/recycle processes.

Slightly shorter charging plateaus under 3.6 V were observed when using the acid washed electrodes. Further SEM analysis of the acid washed electrodes after cycling (Figure S7, Supporting Information) show significant amounts of flake- and flower-like features alongside toroidal particles, which are typically LiOH crystals. LiOH formation is probably caused by residual protons that are not properly washed-off after acid-treatment, which promotes Li_2O_2 hydrolyzation, forming small LiOH crystals.

3. Discussion

Our results show that water can be used as efficient washing agent for the removal of solid deposits of spent electrodes in Li-O_2 cells, drawing advantages in terms of cost compared with other treatments. This is somehow in contrast to a previous study[45] that suggested that acid washing was essential for discharge product removal. In practice, intense bubbling can be observed when washing the used electrodes by acid (Video S1, Supporting Information). In severe cases, electrodes can be torn into fragments. Whereas using water (Figure S8, Supporting Information) makes the bubbling milder, leading to reduced changes of the electrode structure.

The underlying mechanism of the peroxide species removal during washing lies outside the scope of this work, but 2 reactions have been proposed in the LAB literature to account for Li_2O_2 chemical decomposition in aqueous media:[32,46–48]

$$Li_2O_2 + 2H_2O \rightarrow 2LiOH + H_2O_2 \quad (1)$$

$$H_2O_2 \rightarrow H_2O + \frac{1}{2}O_2 \uparrow \quad (2)$$

$$2Li_2O_2 + 2H_2O \rightarrow O_2 \uparrow + 4LiOH \quad (3)$$

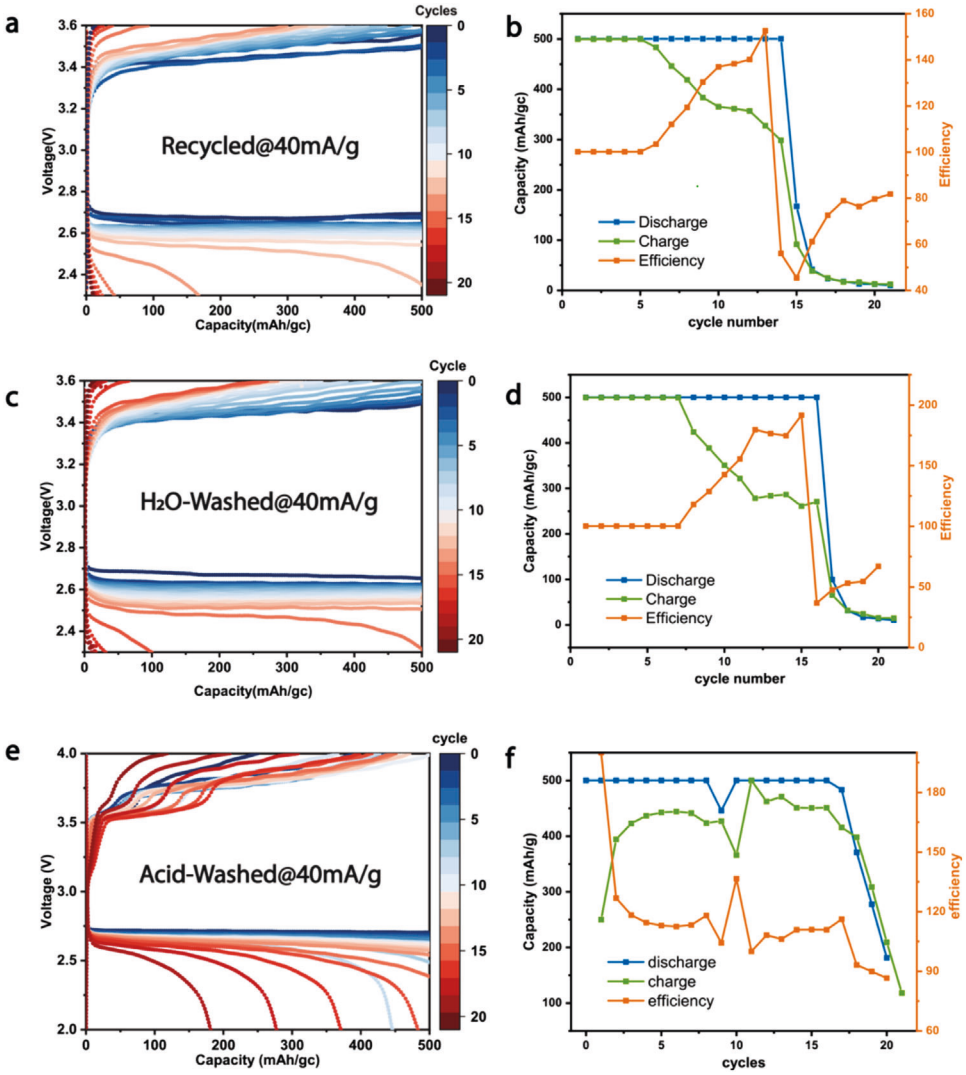

Figure 6. Electrochemistry of recovered electrodes. a,b), c,d), and e,f) cycling voltage profiles and columbic efficiency plots of the recycled, water-washed, and pH = 3 acid-washed electrodes, respectively.

The discharge products can react in two different ways: the lithium peroxide can be first protonated into hydroperoxide and/or into LiOH which further dissolves in the water. Herein, we observe a similar reaction during water and acid-washing. Bubbles could be clearly observed during water-washing of three CNT electrodes (Figure S8, Supporting Information), resulting from the disproportionation of hydroperoxide. This process can be accelerated by vacuum pumping above the washing solvent to extract gasses trapped in the pores (MWCNT hydrophobicity drives to wetting/penetrating issue). Regarding the washing efficiency, most lithium salts can be dissolved in water (Table ST1, Supporting Information). E.g., the solubility of lithium hydroxide is 127 mg mL^{-1}, which means small amounts of water are sufficient to wash the amount of product accumulated (<20 mg) in our cells. Whereas acid washing is more efficient at removing the solid deposits (as it increases the solubility of Li^+) our results indicate that using water can also efficiently wash discharge products via the two steps reaction-dissolution process. Through the above analysis, if carefully eliminated the protons, which can alter the electrochemical reaction, one can generalize such a recycling process to a broader range of products and battery technologies. For instance, as shown in Table ST1 (Supporting Information), the frequently reported products or by-products in Li-O_2 cells (e.g., Li_2CO_3, Li_2O) are soluble or partially soluble in water. A few of these products are basic (e.g., LiOH) and can be removed with acidic aqueous solutions. More generally, other Metal-O_2 batteries such as Na-O_2, Zr-O_2, and Al-O_2 can also benefit from this method as acids can dissolve metal oxides but not carbon matrices.[49,50]

4. Conclusion

This work reports a simple method to prepare binder-free self-standing electrodes form cross-linked MWCNT networks, with high porosity and flexibility. Coiled nanotubes electrodes were made from the MWCNT powder by a three steps process:

ultrasonication, centrifugation, and vacuum filtration. These free-standing electrodes were tested in LOBs showing capacities of ≈1480 mAh g_{CNT}^{-1}, equivalent to more than 3700 Wh kg_{CNT}^{-1} of energy density. We demonstrated that these binder-free electrodes can be treated at end-of-life, by efficiently removing adsorbed species using water or acid solutions, by two methods: a) reconditioning the electrode or b) reclaiming the carbon nanotube and remaking a new electrode. The reconditioned electrodes were then tested for second-life application, showing almost identical electrochemical performance than when freshly prepared. Furthermore, we suggested routes of undergoing reactions of such recycling method and given an outlook of applicability to other metal-O_2 batteries. These findings will be helpful in the development of greener high energy density batteries while reducing recycling costs and environmental impacts.

5. Experimental Section

Self-Standing Electrode Preparation: Free-standing binder-free electrodes were prepared using 20 mg of MWCNT (Nanotech Lab.) powder, added to 750 mL of Isopropanol and dispersed using an ultrasonic probe (Sonoplus UW 2200) with intermittent pulses of 200 W for 30 minutes. The MWCNT solution was then centrifuged in 300 mL bottles at 400 rpm for 45 min. The clear supernatant solute was vacuum filtrated with the GF/C Whatman glassy microfiber filter. The precipitation solution was reused to repeat the procedure a second time. The solution of the second centrifugation became clearer, indicating that the dispersed MWCNT was less concentrated. The filtrated MWCNT was entangled and formed a self-standing porous electrode. Above a MWCNT loading of 2 mg cm^{-2}, the self-standing electrode could be easily peeled off.

The above as-prepared electrodes were dried under vacuum overnight at 120 °C. 16 µm thick Celgard (ENTEK 16 µm) and Whatman (Sigma) separators were similarly dried under vacuum at 70 °C prior to cell assembly. LiTFSI (Sigma–Aldrich), $LiNO_3$ (Alfa Aesar) and dimethylacetamide (Alfa Aesar) were used as received. The water level in the electrolyte was measured at less than 100 ppm by Karl Fischer titration ahead of storing with molecular sieves in an Ar-filled glovebox.

Self-Standing Electrode Reconditioning and Recycling: Reconditioning was performed by soaking the cycled electrodes (after cell death) in a hydrochloric acid or water bath (see Video S1, Supporting Information) for 30 min, inducing bubble formation. The current collector detached from the MWCNT electrodes during the bubbling process. In order to extract the gas trapped in the pores and to impregnate the HCl/H_2O into the structure, vacuum pumping was performed above the liquid. For the recycling, self-standing electrodes were washed in HCl/H_2O and then in ethanol using a Buchner filter. After weighting, the remaining powder was re-dispersed by a similar process shown in Figure 1 to re-form fresh electrodes (with a smaller 2.5 cm of diameter Buchner funnel).

Electrochemical Measurements: Cell construction was done by directly using the filter of the vacuum filtration process with an added Celgard on the anode side, to slow down oxygen percolation to the lithium foil and avoid occasional short circuit issues from CNT percolation through Whatman filters. 100 µL of electrolyte was used. Electrochemical cycling was performed using a Bio-logic VSP. The Pressure Cell setup was developed following the design described by F. Lepoivre et al.[41] Details of the e^-/O_2 ratio calculation can be found in Figure S9 (Supporting Information). A 2 h rest at open-circuit voltage was systematically performed before galvanostatic cycling, thus allowing oxygen diffusion in the electrolyte. A capacity retention comparison with SP@GDL electrodes (Figure S10, Supporting Information) was performed using Whatman glassy fiber separators instead of the Celgard separators to limit wetting issues in SP@GDL electrodes.

Post-Mortem Characterization: *D x-ray imaging (nano-CT)*: Ex situ X-ray nano-holotomography[34] acquisitions were performed at the ESRF ID16B beamline.[51] Four tomographic scans, constituted each of 3203 projections, were recorded on a PCO edge 5.5 camera (2560 × 2160 $pixels^2$) along a 360° rotation with an exposure time of 45 ms per projection using an incident X-ray beam having an energy of 17.5 keV and a high flux of 1.4 10^{11} ph/s^{-1}. The total acquisition time was ≈20 min per full holo-tomography scan. 3D reconstructions were achieved in two steps: (i) phase retrieval calculation using an in-house developed octave script based on a Paganin-like approach using a delta/beta ratio of 303, and (ii) filtered backprojection reconstruction using ESRF software PyHST2,[52] for a final volume of 64 × 64 × 54 μm^2 and a voxel size of 25 nm. For tomography measurements, samples have been carved as small tip using carving a Zeiss Palm laser beam and subsequently retrieved thanks to an epoxy-wetted pencil lead. The cycled electrodes were soaked in dimethylacetamide to leach the salt and then dried in a vacuum without heating.

Raman Spectroscopy Measurements: Dried electrodes were sealed between two glass slides, and 532 nm laser source of 10 mW power with a diaphragm of 50 µm slit was used in the Thermo-Fisher Scientific DXR2 Raman microscope during the acquisition. For each sample in this work, it was collected spectra at ten different areas and for each area averaged 32 spectra of 1 s of exposure time.

SEM/EDX Acquisition: For the SEM, the cycled cathodes were soaked in the solvent DMA to wash the salt in the dry room. After drying naturally, the DMA in the cathodes, were transferred from the dry room to the SEM (FEI quanta-200 F) with an airtight sample holder to avoid contamination. Other washed and recycled electrodes were handled under fume hood.

XPS: XPS analysis was carried out using an Escalab 250XI spectrometer from Thermo Fisher Scientific (West Sussex, UK). The instrument was operating in constant analyzer energy mode. A monochromatic Al-Kα source (1486.74 eV) and a flood gun for charge neutralization were used, with a spot size of 0.9 mm. Survey scans were acquired using pass energy of 100 eV, using 0.5 eV steps. For narrow scans the number of scans was 10, using pass energy of 20 eV and step size of 0.05 eV. The energetic position of the C 1 s emission line (binding energy of 284.6 eV) was chosen to calibrate the energy scale of all spectra.

Supporting Information

Supporting Information is available from the Wiley Online Library or from the author.

Acknowledgements

This research was supported by the French Ministry Higher Education, Research and Innovation. The authors acknowledge the European Synchrotron Radiation Facility for provision of beam time (in-house research time) using the ID16B beamline. They also acknowledge use of the Cambridge XPS System, part of Sir Henry Royce Institute – Cambridge Equipment, EPSRC grant EP/P024947/1 and Dr. Carmen Fernandez-Posada for XPS data acquisition and processing. I.T. and C.P.G. acknowledge funding from the European Research Council (ERC) BATNMR project. A.A.F. acknowledges the European Union's Horizon 2020 research and innovation program for the funding support through the European Research Council (grant agreement 772873, "ARTISTIC" project). A.A.F. acknowledges Institut Universitaire de France for the support. Work performed at the Center for Nanoscale Materials, a U.S. Department of Energy Office of Science User Facility, was supported by the U.S. DOE, Office of Basic Energy Sciences, under Contract No. DE-AC02-06CH11357.

Conflict of Interest

The authors declare no conflict of interest.

Data Availability Statement

The data that support the findings of this study are available in the supplementary material of this article.

Keywords

binder-free, electrochemistry, Li-O_2 batteries, MWCNTs, recyclable materials, self-standing electrodes, x-ray nano-tomography

Received: May 4, 2023
Revised: August 28, 2023
Published online: October 10, 2023

[1] U.S. Global Change Research Program, D. J. Wuebbles, D. W. Fahey, K. A. Hibbard, D. J. Dokken, B. C. Stewart, T. K. Maycock, Global Change Research Program, USA, **2017**.
[2] C. Pillot, The Rechargeable Battery Market and Main Trends, **2018**.
[3] A. Yu, M. Sumangil, Top electric vehicle markets dominate lithium-ion battery capacity growth.
[4] E. A. Olivetti, G. Ceder, G. G. Gaustad, X. Fu, *Joule* **2017**, *1*, 229.
[5] X. Fu, D. N. Beatty, G. G. Gaustad, G. Ceder, R. Roth, R. E. Kirchain, M. Bustamante, C. Babbitt, E. A. Olivetti, *Environ. Sci. Technol.* **2020**, *54*, 2985.
[6] K. Richa, C. W. Babbitt, G. Gaustad, X. Wang, *Resour., Conserv. Recycl.* **2014**, *83*, 63.
[7] A. Mayyas, D. Steward, M. Mann, *Sustain. Mater. Technol.* **2019**, *19*, e00087.
[8] F. Arshad, L. Li, K. Amin, E. Fan, N. Manurkar, A. Ahmad, J. Yang, F. Wu, R. Chen, *ACS Sustainable Chem. Eng.* **2020**, *8*, 13527.
[9] Y. Yang, E. G. Okonkwo, G. Huang, S. Xu, W. Sun, Y. He, *Energy Storage Mater.* **2021**, *36*, 186.
[10] M. Armand, J.-M. Tarascon, *Nature* **2008**, *451*, 652.
[11] D. Larcher, J.-M. Tarascon, *Nat. Chem.* **2015**, *7*, 19.
[12] J. E. Harlow, X. Ma, J. Li, E. Logan, Y. Liu, N. Zhang, L. Ma, S. L. Glazier, M. M. E. Cormier, M. Genovese, S. Buteau, A. Cameron, J. E. Stark, J. R. Dahn, *J. Electrochem. Soc.* **2019**, *166*, A3031.
[13] P. G. Bruce, S. A. Freunberger, L. J. Hardwick, J.-M. Tarascon, *Nat. Mater.* **2012**, *11*, 19.
[14] J. Lu, L. Li, J.-B. Park, Y.-K. Sun, F. Wu, K. Amine, *Chem. Rev.* **2014**, *114*, 5611.
[15] J. Wandt, P. Jakes, J. Granwehr, H. A. Gasteiger, R.-A. Eichel, *Angew. Chem.* **2016**, *128*, 7006.
[16] N. Mahne, B. Schafzahl, C. Leypold, M. Leypold, S. Grumm, A. Leitgeb, G. A. Strohmeier, M. Wilkening, O. Fontaine, D. Kramer, *Nat. Energy* **2017**, *2*, 17036.
[17] A. C. Luntz, B. D. McCloskey, *Nat. Energy* **2017**, *2*, 17056.
[18] J. K. Papp, J. D. Forster, C. M. Burke, H. W. Kim, A. C. Luntz, R. M. Shelby, J. J. Urban, B. D. Mccloskey, *J. Phys. Chem. Lett.* **2017**, *8*, 1169.
[19] R. Black, S. H. Oh, J.-H. Lee, T. Yim, B. Adams, L. F. Nazar, *J. Am. Chem. Soc.* **2012**, *134*, 2902.
[20] A. Halder, H.-H. Wang, K. C. Lau, R. S. Assary, J. Lu, S. Vajda, K. Amine, L. A. Curtiss, *ACS Energy Lett.* **2018**, *3*, 1105.
[21] Z. Su, V. De Andrade, S. Cretu, Y. Yin, M. J. Wojcik, A. A. Franco, A. Demortière, *ACS Appl. Energy Mater.* **2020**, *3*, 4093.
[22] J. Huang, Z. Jin, Z.-L. Xu, L. Qin, H. Huang, Z. Sadighi, S. Yao, J. Cui, B. Huang, J.-K. Kim, *Energy Storage Mater.* **2017**, *8*, 110.
[23] Y. J. Lee, S. H. Park, S. H. Kim, Y. Ko, K. Kang, Y. J. Lee, *ACS Catal.* **2018**, *8*, 2923.
[24] P. Xu, C. Chen, J. Zhu, J. Xie, P. Zhao, M. Wang, *J. Electroanal. Chem.* **2019**, *842*, 98.
[25] J. Liu, D. Li, S. Zhang, Y. Wang, G. Sun, Z. Wang, H. Xie, L. Sun, *J. Energy Chem.* **2020**, *46*, 94.
[26] H. Xue, X. Mu, J. Tang, X. Fan, H. Gong, T. Wang, J. He, Y. Yamauchi, *J. Mater. Chem. A* **2016**, *4*, 9106.
[27] H. Zhang, G. G. Eshetu, X. Judez, C. Li, L. M. Rodriguez-Martínez, M. Armand, *Angew. Chem., Int. Ed.* **2018**, *57*, 15002.
[28] B. J. Bergner, A. Schürmann, K. Peppler, A. Garsuch, J. Janek, *J. Am. Chem. Soc.* **2014**, *136*, 15054.
[29] G. Leverick, M. Tulodziecki, R. Tatara, F. Bardé, Y. Shao-Horn, *Joule* **2019**, *3*, 1106.
[30] J. Lu, Y. Jung Lee, X. Luo, K. Chun Lau, M. Asadi, H.-H. Wang, S. Brombosz, J. Wen, D. Zhai, Z. Chen, D. J. Miller, Y. Sub Jeong, J.-B. Park, Z. Zak Fang, B. Kumar, A. Salehi-Khojin, Y.-K. Sun, L. A. Curtiss, K. Amine, *Nature* **2016**, *529*, 377.
[31] I. Temprano, T. Liu, E. Petrucco, J. H. J. Ellison, G. Kim, E. Jónsson, C. P. Grey, *Joule* **2020**, *4*, 2501.
[32] T. Liu, G. Kim, E. Jónsson, E. Castillo-Martinez, I. Temprano, Y. Shao, J. Carretero-González, R. N. Kerber, C. P. Grey, *ACS Catal.* **2019**, *9*, 66.
[33] T. Liu, M. Leskes, W. Yu, A. J. Moore, L. Zhou, P. M. Bayley, G. Kim, C. P. Grey, *Science* **2015**, *350*, 530.
[34] P. Cloetens, W. Ludwig, J. Baruchel, D. Van Dyck, J. Van Landuyt, J. P. Guigay, M. Schlenker, *Appl. Phys. Lett.* **1999**, *75*, 2912.
[35] T.-T. Nguyen, J. Villanova, Z. Su, R. Tucoulou, B. Fleutot, B. Delobel, C. Delacourt, A. Demortière, *Adv. Energy Mater.* **2021**, 2003529.
[36] Z. Su, E. Decencière, T.-T. Nguyen, K. El-Amiry, V. De Andrade, A. A. Franco, A. Demortière, *npj Comput. Mater.* **2022**, *8*, 30.
[37] S. J. Cooper, A. Bertei, P. R. Shearing, J. A. Kilner, N. P. Brandon, *SoftwareX* **2016**, *5*, 203.
[38] T.-T. Nguyen, A. Demortière, B. Fleutot, B. Delobel, C. Delacourt, S. J. Cooper, *npj Comput. Mater.* **2020**, *6*.
[39] J. Gostick, Z. Khan, T. Tranter, M. Kok, M. Agnaou, M. Sadeghi, R. Jervis, *JOSS* **2019**, *4*, 1296.
[40] Y. Yu, G. Huang, J.-Y. Du, J.-Z. Wang, Y. Wang, Z.-J. Wu, X.-B. Zhang, *Energy Environ. Sci.* **2020**, *13*, 3075.
[41] F. Lepoivre, A. Grimaud, D. Larcher, J.-M. Tarascon, *J. Electrochem. Soc.* **2016**, *163*, A923.
[42] X. Mu, J. Jiang, H. Deng, Y. Qiao, M. Zheng, X. Zhang, P. He, H. Zhou, *Nano Energy* **2019**, *64*, 103945.
[43] W. Yin, A. Grimaud, I. Azcarate, C. Yang, J.-M. Tarascon, *J. Phys. Chem. C* **2018**, *122*, 6546.
[44] J. Lu, S. Dey, I. Temprano, Y. Jin, C. Xu, Y. Shao, C. P. Grey, *ACS Energy Lett.* **2020**, *5*, 3681.
[45] J.-L. Shui, H.-H. Wang, D.-J. Liu, *Electrochem. Commun.* **2013**, *34*, 45.
[46] B. D. Mccloskey, A. Valery, A. C. Luntz, S. R. Gowda, G. M. Wallraff, J. M. Garcia, T. Mori, L. E. Krupp, *J. Phys. Chem. Lett.* **2013**, *4*, 2989.
[47] F. Urbain, V. Smirnov, J.-P. Becker, A. Lambertz, F. Yang, J. Ziegler, B. Kaiser, W. Jaegermann, U. Rau, F. Finger, *Energy Environ. Sci.* **2016**, *9*, 145.
[48] Y. Qiao, S. Wu, Y. Sun, S. Guo, J. Yi, P. He, H. Zhou, *ACS Energy Lett.* **2017**, *2*, 1869.
[49] L. Gaines, *Sustain. Mater. Technol.* **2018**, *17*, e00068.
[50] C. Fang, J. Li, M. Zhang, Y. Zhang, F. Yang, J. Z. Lee, M.-H. Lee, J. Alvarado, M. A. Schroeder, Y. Yang, B. Lu, N. Williams, M. Ceja, L. Yang, M. Cai, J. Gu, K. Xu, X. Wang, Y. S. Meng, *Nature* **2019**, *572*, 511.
[51] G. Martínez-Criado, J. Villanova, R. Tucoulou, D. Salomon, J.-P. Suuronen, S. Labouré, C. Guilloud, V. Valls, R. Barrett, E. Gagliardini, Y. Dabin, R. Baker, S. Bohic, C. Cohen, J. Morse, *J. Synchrotron Rad.* **2016**, *23*, 344.
[52] C. Hintermüller, F. Marone, A. Isenegger, M. Stampanoni, *J. Synchrotron Rad.* **2010**, *17*, 550.

